J. Fluid Mech. (2023), *vol*. 956, A23, doi:10.1017/jfm.2023.15

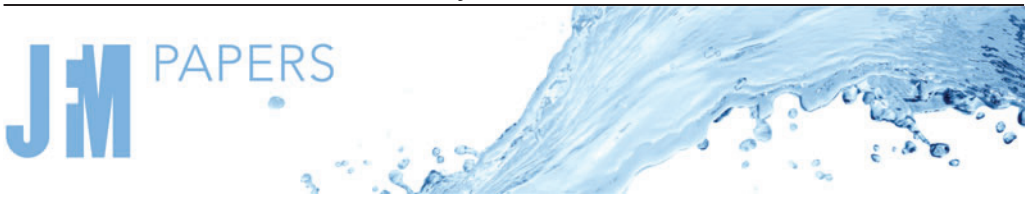

Morphology evolution of a melting solid layer above its melt heated from below

Rui Yang[1,†], **Christopher J. Howland**[1,†], **Hao-Ran Liu**[2,†], **Roberto Verzicco**[1,3,4,†] **and Detlef Lohse**[1,5,†]

[1]Physics of Fluids Group and Max Planck Center for Complex Fluid Dynamics, MESA+ Institute and J. M. Burgers Centre for Fluid Dynamics, University of Twente, P.O. Box 217, 7500AE Enschede, The Netherlands

[2]Department of Modern Mechanics, University of Science and Technology of China, Hefei 230026, China

[3]Dipartimento di Ingegneria Industriale, University of Rome 'Tor Vergata', Roma 00133, Italy

[4]Gran Sasso Science Institute - Viale F. Crispi, 7 67100 L'Aquila, Italy

[5]Max Planck Institute for Dynamics and Self-Organization, 37077 Göttingen, Germany

(Received 15 August 2022; revised 16 December 2022; accepted 27 December 2022)

We numerically study the melting process of a solid layer heated from below such that a liquid melt layer develops underneath. The objective is to quantitatively describe and understand the emerging topography of the structures (characterized by the amplitude and wavelength), which evolve out of an initially smooth surface. By performing both two-dimensional (achieving Rayleigh number up to $Ra = 10^{11}$) and three-dimensional (achieving Rayleigh number up to $Ra = 10^{9}$) direct numerical simulations with an advanced finite difference solver coupled to the phase-field method, we show how the interface roughness is spontaneously generated by thermal convection. With increasing height of the melt the convective flow intensifies and eventually even becomes turbulent. As a consequence, the interface becomes rougher but is still coupled to the flow topology. The emerging structure of the interface coincides with the regions of rising hot plumes and descending cold plumes. We find that the roughness amplitude scales with the mean height of the liquid layer. We derive this scaling relation from the Stefan boundary condition and relate it to the non-uniform distribution of heat flux at the interface. For two-dimensional cases, we further quantify the horizontal length scale of the morphology, based on the theoretical upper and lower bounds given for the size of convective cells known from Wang *et al.* (*Phys. Rev. Lett.*, vol. 125, 2020, 074501). These bounds agree with our simulation results. Our findings highlight the key connection between the morphology of the melting solid and the convective flow structures in the melt beneath.

Key words: Bénard convection, solidification/melting, turbulent convection

† Email addresses for correspondence: r.yang-1@utwente.nl, c.j.howland@utwente.nl, liuhr@ustc.edu.cn, verzicco@uniroma2.it, d.lohse@utwente.nl

1. Introduction

Melting and freezing are important for a wide range of applications across industry, geophysics and astrophysics, such as in aircraft de-icing (Cao, Tan & Wu 2018) and the dynamics of icy satellites (Spencer *et al.* 2006), the Earth's mantle (Labrosse, Hernlund & Coltice 2007), icebergs and ice shelves (Ristroph 2018). These phase transition processes also belong to the wider class of moving free boundary problems (called Stefan problems, Rubinstein 1971), which are very complex because the boundaries of the domains are usually unknown and have to be determined as part of the solution. In particular, the presence of fluid motion modifies the transport of heat which is crucial to the melting and freezing dynamics.

As an important part of the global climate system, the topography of the ice–ocean interface at the base of ice sheets has received increasing attention due to its effects on the ice shelf stability and the basal melt rate (Stanton *et al.* 2013; Jenkins *et al.* 2018; Hewitt 2020; Cenedese & Straneo 2023). Also, in industrial applications such as in latent thermal energy storage devices, the roughness of the basal topography of the phase-change materials has also been found to affect the heat transfer efficiency (Kamkari & Amlashi 2017; Sivasamy, Devaraju & Harikrishnan 2018). However, little is known about the mechanisms responsible for the evolving roughness of the basal solid topography. The interaction between the melting processes and turbulent flows is thus a relevant, interesting and complex problem, in which fluid dynamics and thermodynamics are intimately coupled. The key fundamental question we want to address here is: How does a turbulent convective melt flow beneath the melting solid affect its basal topography? And can one develop a quantitative theory for the evolution of the basal morphology?

A way to answer this question is to start by considering a sufficiently simplified and controllable system that still possesses the complexity and rich phenomenology of the turbulent flow observed in reality. A well-studied and commonly used convection set-up in fluid dynamics is Rayleigh–Bénard (RB) convection (Ahlers, Grossmann & Lohse 2009; Lohse & Xia 2010; Chillà & Schumacher 2012; Shishkina 2021), which considers a fluid layer confined between a cold top and a hot bottom plate. RB convection has previously been taken as model system to study multiphase flows, including studies on convection with dispersed phases (Oresta *et al.* 2009; Kim *et al.* 2020; Liu *et al.* 2022*a*), two-layer convection (Zhong, Funfschilling & Ahlers 2009; Xie & Xia 2013; Liu *et al.* 2022*b*) and convection with phase transitions (Lakkaraju *et al.* 2013; Wang, Mathai & Sun 2019).

Some early experimental studies of a melting solid in RB convection mainly focused on pattern formation at the liquid–solid interface in the presence of a weakly convective flow (Davis, Müller & Dietsche 1984). Since then, more relevant studies have appeared, including both experimental and numerical work to study the effects of convective flow (Favier, Purseed & Duchemin 2019), shear (Couston *et al.* 2021; Hester *et al.* 2021), rotation (Ravichandran & Wettlaufer 2021), initial conditions (Purseed *et al.* 2020) and the density maximum of water at 4 °C (Wang, Calzavarini & Sun 2021*a*; Wang *et al.* 2021*b*,*c*), which reveal the solid topography and its melt rate with convective flow, covering a wealth of phenomena.

However, most of the previous experimental and numerical studies have only considered turbulent but still relatively weak convection (Rayleigh number (Ra) $\leq 10^8$). In many natural and industrial applications, however, the thermal driving can be stronger and the flow more turbulent. Increasing Ra will affect both the flow structures and the heat transfer scaling, e.g. the different heat transfer scalings in the plume impacting region and plume ejecting region in van der Poel *et al.* (2015*b*), Zhu *et al.* (2018) and Reiter *et al.* (2021), and a cross-over in the wall heat transport from impacting dominated to ejecting dominated is

found at $Ra \approx 3 \times 10^{11}$ when $Pr = 1$ (Reiter *et al.* 2021). How highly turbulent convection affects the emerging morphology of the melting substrate remains a crucial but hitherto unsolved question.

In order to better estimate the coupling of turbulent convection to the morphology of the melting solid, in this work, we aim to extend the simulations on melting in the RB configuration to higher Ra (up to 10^9 in three dimensions and up to 10^{11} in two dimensions), by performing direct numerical simulations coupled to the phase-field method. In particular, we focus on the physical mechanism for the formation of roughness, which is due to the different heat flux contributions from impacting and ejecting plumes, and their evolution as the thermal convection strengthens with a scaling of $1/3$ with the effective Ra number.

The paper is organized as follows. In § 2, we describe the governing equations and control parameters used in the simulations. In § 3, we show how the morphology evolves under the interaction with convective flow beneath. In § 4, we quantitatively analyse the scaling of the interface amplitude with Ra. In § 5, we extend this analysis to the evolution of the interface with increasing Ra, characterized by the typical wavelengths. In § 6, we show how the roughness amplitude depends on the Stefan number St, which is the non-dimensional latent heat. Finally, in § 7, we summarize the results and give an outlook to future work.

2. Governing equations and control parameters

The flow in RB convection is confined between two parallel plates separated by a distance H, with gravitational acceleration g acting orthogonally to these plates. We numerically integrate the velocity field $\boldsymbol{u}$ and the temperature field θ according to the Navier–Stokes equations subject to the Oberbeck–Boussinesq approximation, ignoring potential density anomalies which e.g. occur for water at 4 °C. We implement the phase-field method presented by Hester *et al.* (2020) to simulate the melting solid. In this technique, the phase field variable ϕ is integrated in time and space, and smoothly transitions from a value of 1 in the solid to a value of 0 in the liquid. The dimensionless governing equations, constrained by the incompressibility condition $\boldsymbol{\nabla} \cdot \boldsymbol{u} = 0$, read

$$\frac{\partial \boldsymbol{u}}{\partial t} + \boldsymbol{u} \cdot \boldsymbol{\nabla} \boldsymbol{u} = -\boldsymbol{\nabla} p + \sqrt{\frac{Pr}{Ra}} \nabla^2 \boldsymbol{u} - \frac{\phi \boldsymbol{u}}{\eta} + \theta \boldsymbol{e}_z, \tag{2.1}$$

$$\frac{\partial \theta}{\partial t} + \boldsymbol{u} \cdot \boldsymbol{\nabla} \theta = \frac{1}{\sqrt{RaPr}} \nabla^2 \theta + St \frac{\partial \phi}{\partial t}, \tag{2.2}$$

$$\frac{\partial \phi}{\partial t} = \frac{6}{5StC\sqrt{RaPr}} \left[\nabla^2 \phi - \frac{1}{\epsilon^2} \phi (1 - \phi)(1 - 2\phi + C\theta) \right]. \tag{2.3}$$

Here, the temperature field $\theta = (T - T_m)/\Delta$ has been non-dimensionalized using the temperature difference Δ between the plates and the equilibrium melting temperature T_m, and the velocity field $\boldsymbol{u}$ has been non-dimensionalized with the free-fall velocity $U_f = \sqrt{g\beta H \Delta}$, where β is the thermal expansion coefficient; $\boldsymbol{e}_z$ is the direction of gravity and η is the penalty parameter to damp the velocity to zero in the solid phase, which we set equal to the time step, following Favier *et al.* (2019). All lengths have been made non-dimensional with the plate separation H. The physical control parameters in the

equations are the Rayleigh, Prandtl and Stefan numbers, defined as

$$Ra = \frac{\beta g \Delta H^3}{\nu\kappa}, \quad Pr = \frac{\nu}{\kappa}, \quad St = \frac{\mathcal{L}}{c_p \Delta}. \tag{2.4a–c}$$

Here, ν is the kinematic viscosity of the liquid, κ is the thermal diffusivity (which is assumed to be equal in the solid and the liquid), g is the gravitational acceleration, c_p the specific heat and $\mathcal{L}$ the latent heat; Pr is fixed to 10, representative of cold water. First, St is fixed to 1, and the effect of increasing St to somewhat more realistic values (in practical situations) for ice and other phase-change materials will be investigated in § 6.

The applied phase-field model was initially derived based on entropy conservation, which guarantees the thermodynamic consistency, and also satisfies the Gibbs–Thompson relation (Hohenberg & Halperin 1977; Wang *et al.* 1993; Favier *et al.* 2019; Hester *et al.* 2020), which is given by

$$\frac{T - T_m}{\Delta} = \frac{\varepsilon}{C}\gamma, \tag{2.5}$$

where T is the dimensional temperature, T_m the equilibrium melting point, γ the local interface curvature and ε is used to measure the diffuse interface thickness; $\epsilon = \varepsilon/H$ is typically chosen as an empirical value in the phase-field method (Ding, Spelt & Shu 2007; Yue, Zhou & Feng 2010). Here, we take ϵ to be equal to the grid spacing in our simulations, following the convergence test in Favier *et al.* (2019). Also, C is the same parameter as appears in (2.3). It controls the dependence of the melting point on the interface curvature. At scales relevant for turbulent convection, we anticipate the Gibbs–Thomson effect to be minimal, because the local curvature is relatively low, and therefore we choose $C = 1$ (Hester *et al.* 2020). The condition of heat flux balance at the liquid–solid interface is given by the classical Stefan conditions (Woods 1992; Worster, Batchelor & Moffatt 2000) as

$$\mathcal{L} v_n = c_p \kappa (\partial_n T^{(S)} - \partial_n T^{(L)}), \tag{2.6}$$

where v_n is the normal velocity of the interface, and the superscripts (S) and (L) represent the solid and liquid phases, respectively. A more detailed discussion of the parameters and the validation of our implementation can be found in Hester *et al.* (2020) and also our own software documentation (Howland 2022).

Three-dimensional (3-D) simulations are conducted in a domain with $(L_x, L_y, L_z) = (2, 1, 1)$, where L_x, L_y and L_z are the dimensionless horizontal lengths in the x direction, y direction and the dimensionless vertical length in the z direction, respectively. Two-dimensional (2-D) simulations are conducted in a domain with $(L_x, L_z) = (2,1)$. We also ensure that there are enough grid points to capture the turbulent flow. Specifically, for the 3-D case of $Ra = 10^9$, we use a uniform mesh of $1536 \times 768 \times 768$. Besides, a grid independence test has been conducted to ensure that the same final conclusion is obtained when the grid size is either halved or doubled. A list of all simulation cases is shown in table 1.

We impose a fixed temperature $\theta = 1$ at the bottom heated plate (below the melt) and $\theta = 0$ at the top cooled plate (above the frozen liquid), and no-slip boundary conditions for both plates. Periodic boundary conditions are imposed in horizontal directions. The melting temperature of the solid is set to the same value as the temperature at the top wall $\theta = 0$. Initially, we prescribe a flat interface height at $h/H = 0.1$, with the velocity field set to $\boldsymbol{u} = 0$ everywhere. The temperature field in the liquid is initialized as a linear profile

Ra^0_{eff}	Ra	St	Resolution	Discussed in
		3-D		
10^5	10^8	1	$768 \times 384 \times 384$	§ 4
10^6	10^9	1	$1536 \times 768 \times 768$	§§ 3, 4
		2-D		
10^5	10^8	[0.25,1,4]	288×576	§§ 4, 5, 6
10^6	10^9	[0.1,0.2,0.25,1,4]	576×1152	§§ 4, 5, 6
10^7	10^{10}	[0.25,1,4]	1152×2304	§§ 4, 5, 6
10^8	10^{11}	1	2304×4608	§§ 4, 5

Table 1. List of all simulation cases. Here, Ra^0_{eff} is the effective Ra defined by the initial liquid layer height.

with random fluctuations of maximal amplitude 0.01 to trigger a transition to turbulence. Simulations are performed using the second-order staggered finite difference code AFiD (Verzicco & Orlandi 1996; van der Poel *et al.* 2015*a*), which has already been extensively validated (Kooij *et al.* 2018) and used to study a wide range of convection problems (van der Poel *et al.* 2015*b*; Yang, Verzicco & Lohse 2016; Yang *et al.* 2020; Wang, Lohse & Shishkina 2021*d*). The extension of the AFiD code to include two phases approached with the phase-field method (Cahn–Hilliard equation) was discussed and validated in Liu *et al.* (2021).

For studying the evolution of the interface topography, the location of the interface, defined implicitly by $\phi = 1/2$, is the key response of the system. Locally, we thus define the dimensionless height of the interface $\xi(x, y, t) = h/H$ by the equation $\phi(x, y, \xi(x, y, t), t) = 1/2$. From that, we infer the dimensionless mean height of the fluid layer as

$$\bar{\xi}(t) = \frac{1}{L_x L_y} \int_0^{L_y} \int_0^{L_x} \xi(x, y, t)\, \mathrm{d}x\, \mathrm{d}y. \tag{2.7}$$

We denote all horizontally averaged values with an overbar. We can use $\bar{\xi}(t)$ to define the effective Rayleigh number of the fluid layer

$$Ra_{eff}(t) = \frac{\beta g \Delta (\bar{h}(t))^3}{\nu\kappa} = Ra(\bar{\xi}(t))^3 \leq Ra. \tag{2.8}$$

We also define the (non-dimensionalized) local heat flux q at the interface as

$$q(x, y, t) = -\frac{K(\nabla T \cdot \boldsymbol{n})|_{Z=h}}{K\Delta/\bar{h}} = -\bar{\xi}(\nabla\theta \cdot \boldsymbol{n})|_{z=\xi}, \tag{2.9}$$

where Z and z denote the dimensional and dimensionless vertical coordinate, respectively, $K = \alpha\rho C_p$ denotes the thermal conductivity and C_p the specific heat; $\boldsymbol{n}$ denotes the normal direction to the solid–liquid interface, calculated by $\boldsymbol{n} = \nabla\phi/|\nabla\phi|$. The time-dependent global Nusselt number is defined as

$$Nu(t) = \bar{q}(t) = -\bar{\xi}\overline{(\nabla\theta \cdot \boldsymbol{n})}|_{z=\xi}. \tag{2.10}$$

Note that calculating such a diffusive flux directly at $\phi = 0.5$ in a phase-field simulation will result in an erroneously small flux since the temperature gradient is smoothed out by the diffuse interface. It is therefore vital to resolve the conductive sublayer, where normal temperature gradients are uniform, outside the diffuse interface region so that the

heat flux can be accurately calculated. We have further validated our interfacial heat flux calculations against the Stefan condition (2.6) to ensure self-consistency.

3. Roughness evolution

First, we study how the morphology of the initially smooth solid layer above the turbulent convective flow evolves during the melting process. The simulations are run until the layer is completely molten. We present an instantaneous 3-D visualization of the temperature field in figure 1(*a*). Vertical slices of the temperature field at various times are shown in figure 1(b-d) along with corresponding bottom views of the interface in figure 1(*e–g*). As seen from these latter figures, the roughness increases as the convective flow intensifies with time. Here, by roughness we refer to the scale of the undulations in the solid–liquid interface. At the early stage, under the influence of convection, the interface evolves from flat to small-scale cellular structures, as shown in figure 1(*e*). Over time, the cellular structures merge and become larger. The large-scale circulation driven by the convection also grows in scale as time evolves. Furthermore, from figures 1(*d*) and 1(*g*), at large Ra_{eff}, we do not find isolated cusps above the sinking plumes as in Favier *et al.* (2019) for smaller Ra_{eff}, but rather more rough topography from recirculation induced melting. We found that the rough cellular structures exist mainly in the regions associated with descending cold plumes while a smoother surface emerges in the region dominated by the rising hot plumes.

Apparently, the interface topography changes as Ra_{eff} increases, depending on the rising hot plume region and the descending cold plume region. This also occurs in two dimensions, as highlighted for example by figure 2 for $Ra = 10^{11}$: at the early stage, the solid melts locally above the rising hot plume, but less so above the descending cold plume. The unstable descending cold plumes locally generate recirculation flow, as shown in figure 2(*a*) where $Ra_{eff} = 3.1 \times 10^8$. While the solid keeps melting and Ra_{eff} increases further, the solid above the cold descending plumes melts faster and becomes rougher than that above the hot rising plumes (see figure 2(*b*) at $Ra_{eff} = 5.3 \times 10^{10}$). More unstable cold plumes generate multiple recirculation flows. These turbulent plumes are able to effectively mix their surroundings, thus inducing an increase of the vertical and horizontal heat transport, therefore resulting in more local roughness elements. The early appearance of the recirculation in figure 2(*a*) was not observed by the previous study of Favier *et al.* (2019). Note that we only have 2-D simulations at high *Ra*. Reiter *et al.* (2021) suggest that the higher *Ra* used in our study is needed to observe the recirculation. The formation of quasi-steady rolls from the normal mode initial condition of Favier *et al.* (2019) leads to coherent interfacial cusps that may also act to inhibit the emergence of such recirculation zones.

4. Roughness amplitude

To quantitatively analyse the topography as time evolves, we first denote the fluctuation terms by a prime, calculated by the local value minus the horizontally averaged value, both for the interface height ξ and heat flux q

$$\xi'(x, y, t) = \xi(x, y, t) - \bar{\xi}(t), \quad q'(x, y, t) = q(x, y, t) - \bar{q}(t), \tag{4.1a,b}$$

where $\bar{q} \equiv \bar{\xi}\,\partial\bar{\theta}/\partial z$. Then we measure the typical amplitude of the interface by the root mean square (r.m.s.) of ξ' as

$$\xi_{rms}(t) = \sqrt{\overline{(\xi(x, y, t) - \bar{\xi}(t))^2}} = \sqrt{\overline{\xi'(x, y, t)^2}}. \tag{4.2}$$

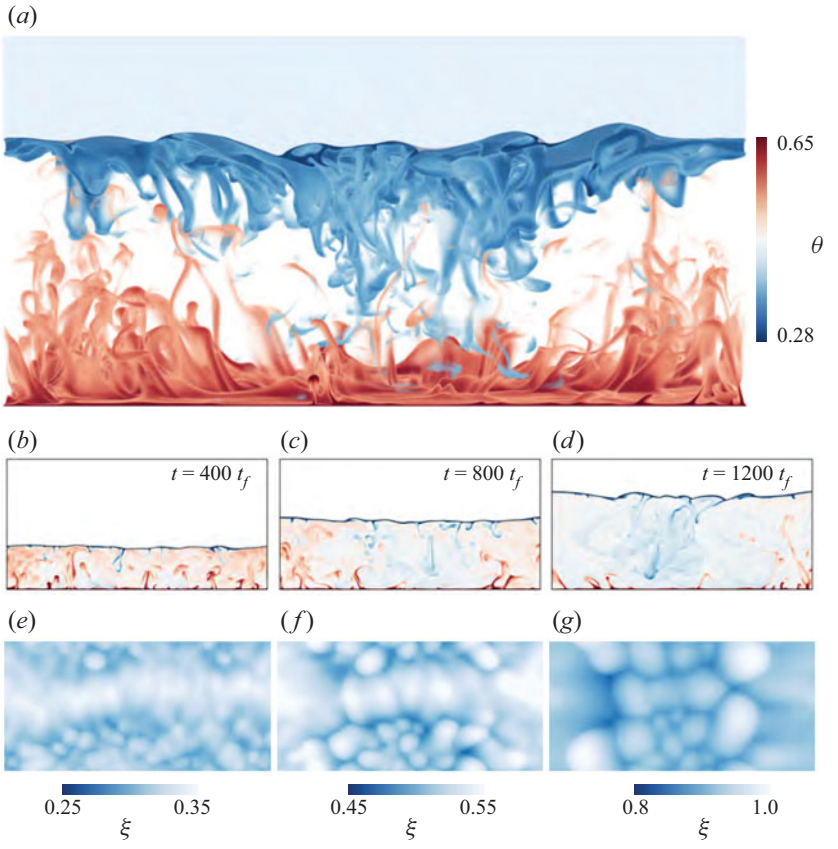

Figure 1. Visualizations of the 3-D numerical simulation at $Ra = 10^9$. (*a*) Instantaneous 3-D temperature field at $t = 1200t_f$. Light blue colour above the flow field represents the solid ice phase $\phi > 1/2$. (*b–d*) Two-dimensional slices of the temperature field at times $400t_f$, $800t_f$ and $1200t_f$, where $t_f = \sqrt{H/g\beta\Delta}$ is the free-fall time. (*e–g*) The contour maps of the solid interface corresponding to the times in (*b–d*). The topography is found to become rougher as time evolves. Note the different colour code in (*g*) as compared with (*e*) and (*f*), reflecting the roughening of the structure with time.

We rescale ξ_{rms} as $\tilde{\xi}_{rms} = \xi_{rms}Ra^{1/3}$ to provide a more general comparison across the different simulations. This is equivalent to non-dimensionalizing the r.m.s. height with the intrinsic length scale $l = (\nu\kappa/g\beta\Delta)^{1/3}$ rather than with H. Figure 4(*a*) shows $\tilde{\xi}_{rms}$ as function of the effective Rayleigh number Ra_{eff}. The amplitude monotonically increases as Ra_{eff} increases. Deforming cellular structures during merging will cause fluctuations in the results. However, we find that $\tilde{\xi}_{rms}$ depends primarily on the effective Rayleigh number, with a reasonable collapse of the data from all of our simulations, following an approximate scaling of ${Ra_{eff}}^{1/3}$.

We now set out to understand this scaling $\tilde{\xi}_{rms} \sim {Ra_{eff}}^{1/3}$. We begin from the non-dimensionalized Stefan boundary condition (2.6), approximated by only the vertical component of the heat flux

$$St\frac{\partial \xi}{\partial t} = -\frac{1}{\sqrt{RaPr}}\frac{\partial \theta}{\partial z} = \frac{1}{\sqrt{RaPr}}\frac{q}{\bar{\xi}}, \tag{4.3}$$

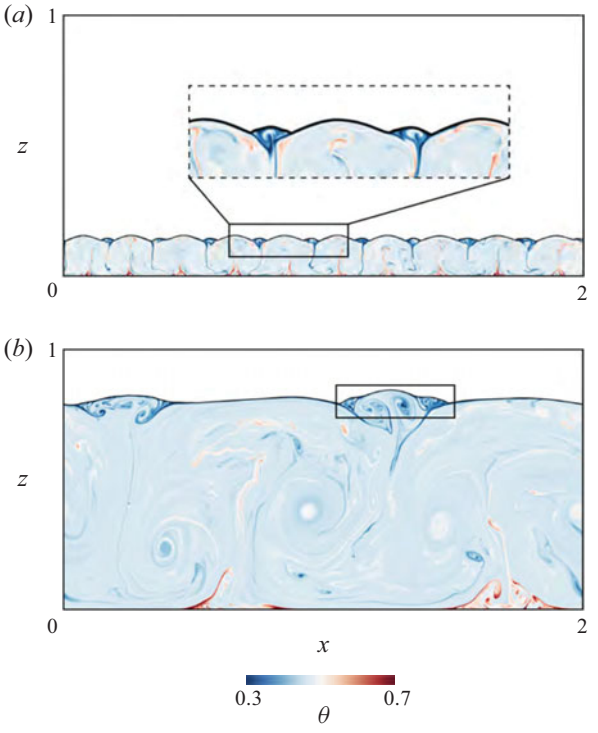

Figure 2. (*a*) Temperature field at $Ra_{eff} = 3.1 \times 10^8$ of 2-D simulation at $Ra = 10^{11}$, with a zoom plot of the interface shape. (*b*) Temperature field at later time at $Ra_{eff} = 5.3 \times 10^{10}$, again for 2-D simulation at $Ra = 10^{11}$.

which relates the melt rate to the local heat flux q using (2.9). Spatial averaging of (4.3) gives

$$\frac{\mathrm{d}\bar{\xi}}{\mathrm{d}t} = \frac{1}{St\sqrt{RaPr}}\frac{\bar{q}}{\bar{\xi}}. \tag{4.4}$$

By assuming that $\xi' \ll \bar{\xi}$, cancelling out the global balance (4.4) from (4.3) and using (4.1*a*,*b*), we obtain

$$\frac{\partial \xi'}{\partial t} \approx \frac{1}{St\sqrt{RaPr}}\frac{q'}{\bar{\xi}}. \tag{4.5}$$

Since Ra_{eff} is solely a function of t, as seen in (2.8), we can use the chain rule to transform the time derivative to one with respect to Ra_{eff} and apply (2.8), (4.4) and (4.5), which gives

$$\begin{aligned}\frac{\partial \xi'}{\partial Ra_{eff}} &= \frac{\partial \xi'}{\partial t}\frac{\partial t}{\partial \bar{\xi}}\frac{\partial \bar{\xi}}{\partial Ra_{eff}} \approx \left(\frac{1}{St\sqrt{RaPr}}\frac{q'}{\bar{\xi}}\right)\left(St\sqrt{RaPr}\frac{\bar{\xi}}{\bar{q}}\right)\left(\frac{1}{3Ra\bar{\xi}^2}\right)\\ &= \frac{q'}{3\bar{q}}Ra_{eff}{}^{-2/3}Ra^{-1/3}.\end{aligned} \tag{4.6}$$

By integrating (4.6), we obtain

$$\xi' \approx \int \frac{q'}{3\bar{q}}Ra_{eff}{}^{-2/3}Ra^{-1/3}\,\mathrm{d}Ra_{eff}. \tag{4.7}$$

What remains unknown in this expression is the normalized heat flux fluctuation $q'/\bar{q}$, and in particular its dependence on Ra_{eff}. Note that in classical turbulent RB convection, it has been found that close to the bottom plate the relative heat transport contributions of the cold descending plume region and the hot rising plumes region are not equal (Zhu *et al.* 2018). As Ra increases there is a cross-over in these heat flux contributions, and the heat flux from the descending plumes can become dominant at high Ra (Reiter *et al.* 2021), as there the thermal boundary layer has become very thin.

Here, we also measure the instantaneous interfacial heat flux for regions associated with the descending cold and rising hot plume regions at different Ra_{eff}, since Ra_{eff} keeps increasing as the solid melts. Thus we can understand the relation between the roughness and the flow structure underneath. Whereas previous studies (Blass *et al.* 2021; Reiter *et al.* 2021) relied on time averaging to distinguish the separate regions, we must use instantaneous snapshots due to our time-evolving fluid domain. We measure the temperature close to the bottom plate at a distance of 10 grid points and identify the local temperature maxima, as highlighted in figure 3(*b*). Note that the exact value of this height does not matter, and our results are robust to changes in this value. The corresponding local heat flux q is plotted in figure 3(*c*), which reflects the similar behaviour of spatial variation of interface heat flux, leading to the morphology evolution. Note the narrow local peaks in q within the cold plume region, which correspond to the recirculation regions forming secondary cusps at the interface. We then prescribe equally sized areas centred at these peaks such that half of the domain is classified as the 'rising hot plume' region. The rest of the domain is classified as the 'descending cold plume' as shown on the temperature snapshot of figure 3(*a*). Five consecutive snapshots are chosen to average the conditionally averaged heat flux.

Then we plot the conditionally averaged heat flux as a function of Ra_{eff} in figure 4(*b*). The heat flux contributions remain approximately constant over a wide range from $Ra_{eff} = 10^6$ to $Ra_{eff} = 10^{10}$. The heat flux fluctuation $q'/\bar{q}$ over the interface can be estimated by the difference between that from the hot rising plume region and that from the cold descending plume region. We do not observe any pronounced dependence on Ra_{eff} so that we can approximate

$$\frac{q'}{\bar{q}} \approx \text{const.} \tag{4.8}$$

By substituting (4.2) and (4.8) into (4.7), we finally obtain the scaling for the r.m.s. of ξ

$$\tilde{\xi}_{rms}(t) = Ra^{1/3}\sqrt{\overline{\xi'(x,y,t)^2}} \sim Ra_{eff}^{1/3}, \tag{4.9}$$

which is consistent with the results in figure 4(*a*). This scaling in turn implies that the (dimensional) r.m.s. height is proportional to the mean height, that is

$$h_{rms} \sim \bar{h}. \tag{4.10}$$

This suggests that the large-scale circulation, determined by the layer thickness $\bar{h}$, has the strongest effect on the roughness amplitude. At $Ra_{eff} > 10^{10}$, $\tilde{\xi}_{rms}$ shows a deviation from the $Ra_{eff}^{1/3}$ scaling, which could be because of a gradual change of the heat flux distribution in hot and cold plume regions as Ra further increases (similar to what was seen by Reiter *et al.* (2021) at $Pr = 1$). We could also associate this with the growing importance of the recirculation regions shown in figure 2(*b*) compared with the large-scale circulation. Such high Rayleigh numbers are not easily achievable with current computational resources but deserve further studies in the future.

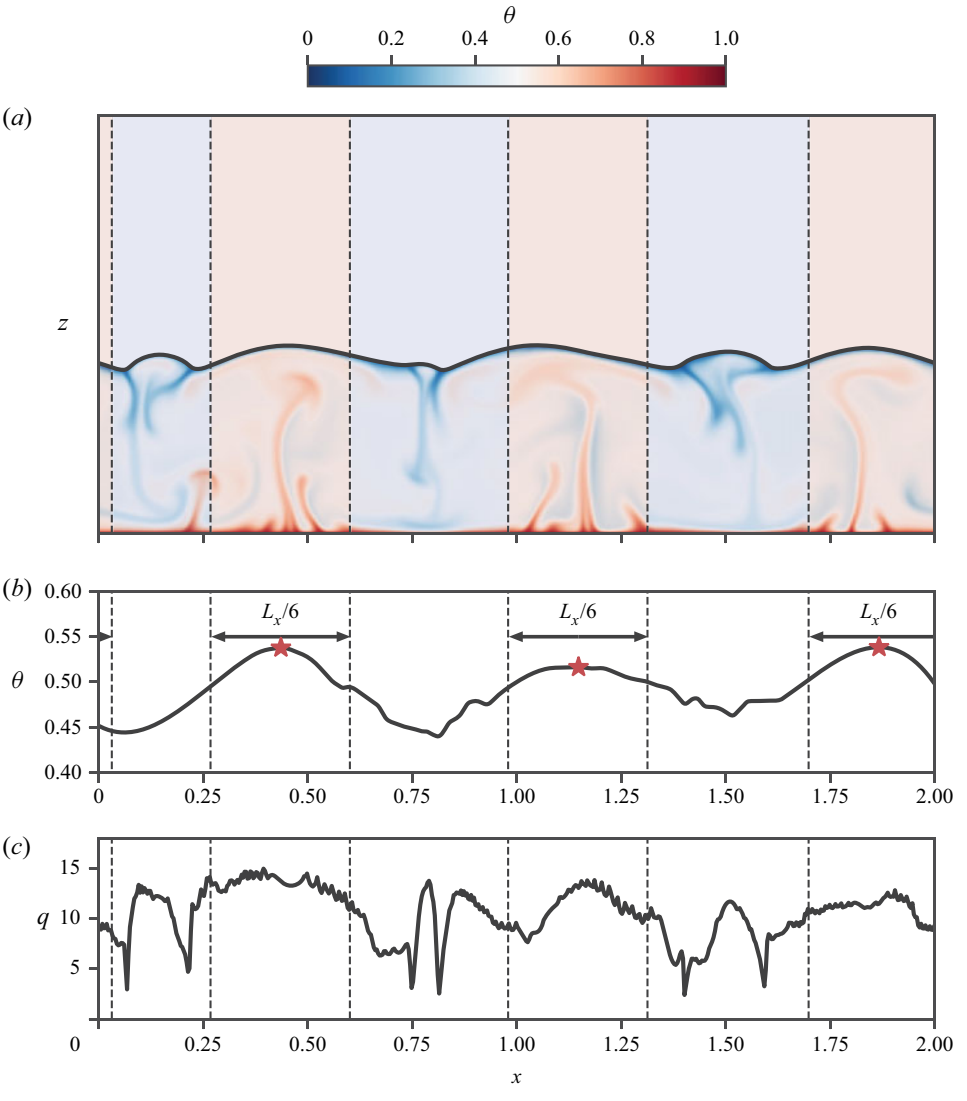

Figure 3. (*a*) An illustration of the temperature field and the separated region. The dashed lines represent the edge of the hot rising (in red colour) and cold descending (in blue colour) plume regions. (*b*) The corresponding temperature distribution as a function of horizontal distance close to the bottom plate at a distance of 10 grid points. The temperature distribution is smoothed by a spatial moving average for each snapshot to avoid instantaneous fluctuations. The red stars represent the measured peak points. Each hot plume region has the same width. (*c*) The corresponding surface heat flux $q(x)$ calculated at the phase boundary, as defined in (2.9), as a function of horizontal distance. The effective Rayleigh number for this snapshot is 7.5×10^6.

5. Roughness wavelength

Another quantity of interest is the typical horizontal scale of the topography. As we shall describe, the circulating flow structures that strongly impact the interface evolution are quite different in 2-D and 3-D simulations, so we choose to analyse them separately.

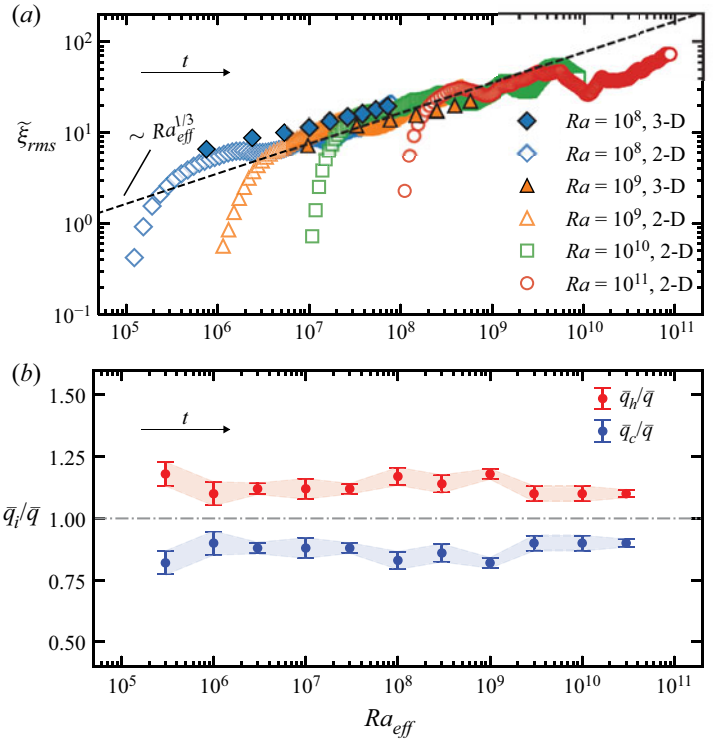

Figure 4. (*a*) Rescaled topography amplitude $\widetilde{\xi}_{rms} = \xi_{rms} Ra^{1/3}$ as a function of the Ra_{eff} (which grows with time) for different global Rayleigh numbers and both 2-D and 3-D simulations. The dashed line shows the $\widetilde{\xi}_{rms} \sim Ra_{eff}^{1/3}$ scaling, derived from (4.3) to (4.9). (*b*) The conditionally averaged heat fluxes averaged over the hot plume region $\bar{q}_h$ and over the cold plume region $\bar{q}_c$ at the interface separately, normalized by the global heat flux at the interface $\bar{q}$. These distinct regions are highlighted in figure 3. Here, the data points are averaged over the five consecutive snapshots around the corresponding Ra_{eff} for 2-D cases. The error bars denote the range of values obtained from these snapshots.

5.1. *Two-dimensional simulations*

Focusing mainly on the 2-D simulations, we consider an integral length scale based on the spatial Fourier transform of the interface height $\hat{h}(k, t)$, where non-dimensional k is the wavenumber. Analogous to the typical definition for turbulence, the typical length scale of the topography can then be estimated as $\lambda(t)/H = 2\pi/k(t)$, which is defined as

$$\frac{\lambda(t)}{H} = \frac{\displaystyle\int_0^\infty k^{-1} |\hat{h}(k, t)|^2 \, \mathrm{d}k}{\displaystyle\int_0^\infty |\hat{h}(k, t)|^2 \, \mathrm{d}k}. \tag{5.1}$$

The length scale $\lambda(t)/H$ is plotted in figure 5(*a*) as a function of $\bar{\xi}(t)$ for different Ra. As expected, the length scale increases with fluctuations due to the merging cellular structures.

The horizontal scale of the topography is expected to correspond to the wavelength of the underlying convective rolls (Esfahani *et al.* 2018; Favier *et al.* 2019). To quantitatively describe the convection rolls, we use the result of Wang *et al.* (2020) for the lower and upper bounds on the aspect ratio of the convective rolls $\Gamma_r = \lambda_r/\bar{h}$, which was derived

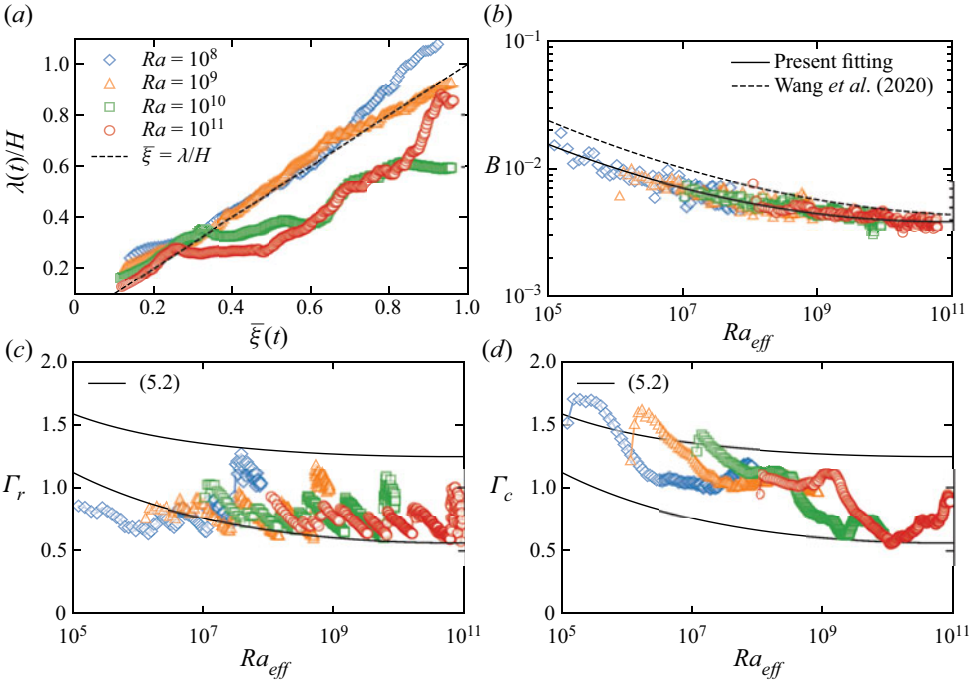

Figure 5. (*a*) The wavelength $\lambda(t)/H$ of the topography as function of interface height $\bar{\xi}(t)$ for different Ra. The dashed line represents $\lambda/H = \bar{\xi}$. For low Ra, λ is always larger than $\bar{\xi}$, while for high Ra, λ can be smaller than $\bar{\xi}$, which means that the topography becomes even rougher. (*b*) Quantity B (defined in (5.3)) as function of Ra_{eff} for different Ra. The solid line represents the quadratic fit of our data, and the dashed line represents the fitting curve from Wang *et al.* (2020). (*c*) The measured convection roll aspect ratio Γ_r as a function of Ra_{eff}, the lower and upper solid lines represent the lower and upper bounds from the theoretical analyses (5.2) of Wang *et al.* (2020). (*d*) The measured interface cell aspect ratio Γ_c as a function of Ra_{eff}, the lower and upper solid lines again represent the lower and upper bounds for interface cells from the theoretical analysis (5.2).

for smooth plates and no slip boundary conditions. Here, λ_r is the wavelength of the convective rolls in classical 2-D RB convection, namely

$$c\sqrt{B} \le \Gamma_r \le \sqrt{1 + 2\sqrt{3B}}/\sqrt{1 - 2\sqrt{3B}}, \tag{5.2}$$

with

$$B \equiv Re^2 Pr^2 Ra^{-1}(\bar{q} - 1)^{-1}, \tag{5.3}$$

where Re is the Reynolds number and c is a constant with $c = 9$, following Wang *et al.* (2020), and $\bar{q}$ is the averaged heat flux. These upper and lower bounds were derived based on the strain–vorticity balance and a generalized Friedrichs inequality (Wang *et al.* 2020). In these 2-D flows, the flow can be assumed as a set of elliptical rolls with a certain range of aspect ratios and the balance between strain and vorticity is determined by the elliptical shape of these rolls. The value of B according to (5.3) is calculated from our simulations and plotted in figure 5(*b*). It can be fitted by $B = 0.45 Ra_{eff}^{-0.38+0.0175\log_{10}(Ra_{eff})}$. The form of this expression comes from a quadratic fit of the data for $\log B$ as a function of $\log Ra_{eff}$, again as obtained by Wang *et al.* (2020) for smooth walls. In figure 5(*c*), we plot the convective roll aspect ratio Γ_r as function of Ra_{eff} and the upper and lower bounds based on (5.2). As expected, Γ_r lies in between them, especially for high Ra_{eff}.

At low Ra_{eff}, disagreements arise since the rough topography is more closely coupled to the convective roll structure, compared with the smooth case in Wang *et al.* (2020), as highlighted by figure 2(*a*). This can cause smaller aspect ratio rolls to 'lock-in' to the shape of the interface and delay the merging of rolls. When beyond $Ra = 10^{11}$, B becomes more horizontal, the upper and lower limits will approach constant values.

We can define a similar aspect ratio $\Gamma_c = \lambda/\bar{h}$ for the cellular structures on the solid–liquid interface. In figure 5(*d*), we plot the interface cell aspect ratio Γ_c as a function of Ra_{eff}, which also shows good agreement with the upper and lower bounds based on (5.2). This means that the horizontal scales of the topography correspond to those of the convective rolls beneath. While considering that one single cellular structure can include either one or two convective rolls (see figures 2*a* and 2*b*), Γ_c can be larger than the upper bounds. It is noted that we only compared with the 2-D simulations, since the theory of Wang *et al.* (2020) is also limited to two dimensions. Also, the theory is no longer applicable once the ice topography has larger deformation, as it is a theory for flat plates.

5.2. *Three-dimensional simulations*

We now turn to the 3-D simulations, where the above theoretical bounds do not apply. In their study of large aspect ratio RB convection, Krug, Lohse & Stevens (2020) observe typical 'superstructures' of aspect ratio $\Gamma = 6.3$ in the temperature and velocity fields at $Ra = 10^8$, $Pr = 1$, along with an increasing trend for the aspect ratio with Ra. These structures significantly exceed the aspect ratios permitted for the rolls in two dimensions, and Pandey, Scheel & Schumacher (2018) find that in three dimensions for Pr closer to 10, even wider rolls can be expected than for $Pr = 1$.

For our 3-D simulations, we can construct similar length scales for the interface as in (5.1). In figure 6, we present two such length scales computed using either Fourier transform in x or y and then averaging over the remaining horizontal axis to give a single scale. For example, the typical interface wavelength in x is defined as

$$\lambda_x(y,t) = \frac{\displaystyle\int_0^\infty k^{-1}|\hat{h}(k,y,t)|^2\,\mathrm{d}k}{\displaystyle\int_0^\infty |\hat{h}(k,y,t)|^2\,\mathrm{d}k}, \quad \overline{\lambda_x}(t) = \frac{1}{L_y}\int_0^{L_y} \lambda_x\,\mathrm{d}y. \tag{5.4a,b}$$

Since the RB system has no preferential flow direction in the horizontal, if the domain were infinitely large one would expect $\lambda_x \approx \lambda_y$ due to rotational symmetry. However, it is clear from figure 6(*a*) that the topography length scales do not match. Comparing the superstructure results of Krug *et al.* (2020) with our domain size, with $L_x/H = 2$ and $L_y/H = 1$, it is not surprising that the aspect ratio of the domain appears to be limiting the scale of the topography. Even for the first recorded snapshot, as shown in figure 6(*b*) with a black dashed line, the aspect ratio of the domain in the y-direction is less than 5, suggesting that large-scale structures expected in unconfined domains could not be reproduced.

As in three dimensions, the large-scale circulation associated with these thermal structures appears to play an important role in the evolution of the interface. We can highlight this in more detail by considering the time-averaged flux of heat at the bottom plate and the phase boundary. We define the time-averaged vertical heat flux at the lower plate as

$$\tilde{q}(x,y) = \frac{1}{t_a}\int_0^{t_a} \frac{H}{\Delta}\frac{\partial T}{\partial z}\,\mathrm{d}t, \tag{5.5}$$

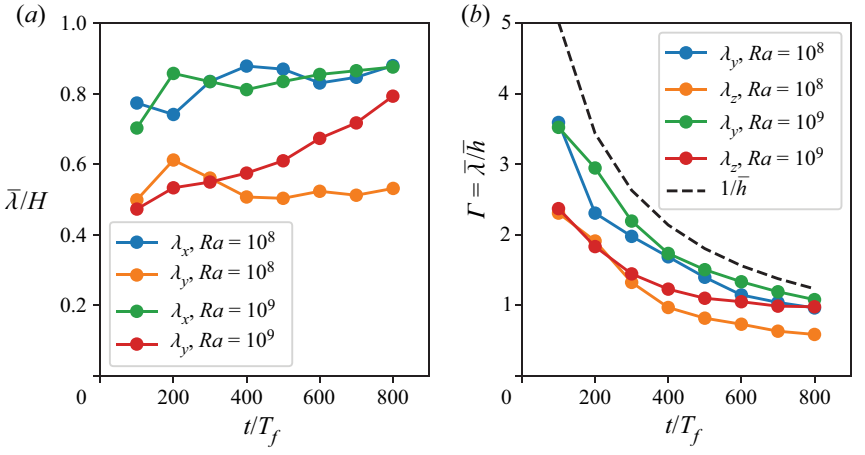

Figure 6. (*a*) Phase boundary horizontal length scales and (*b*) aspect ratios for the 3-D simulations. The large values and the difference between λ_x and λ_y suggest that the domain size is restricting the pattern formation on the interface.

for an averaging time of t_a. For the upper boundary, we can use the local interface height as a proxy for the time-integrated heat flux through $h \approx h_0 + t_a\tilde{q}/(St\sqrt{RaPr})$. To ensure the fluxes are comparable in magnitude, we rescale this upper heat flux to account for the heating of the expanding liquid layer in the simulation. The time-averaged heat fluxes at each boundary are presented in figure 7 for a range of integration times. Particularly at early times, the fluxes at the two boundaries are inversely correlated, with larger heat flux at the top boundary (and hence more melting), corresponding to regions where the integrated heat flux at the lower boundary is smaller.

This can again be associated with the large-scale circulation of RB convection into 'impacting' and 'ejecting' regions. Considering panels (*c*) and (*d*) of figure 7, where the bottom plate shows a region of low heat flux around $y \approx 0.6$. At the Rayleigh numbers being considered, this can be associated with a region where the plumes are ejected from the lower plate. Since the plumes rise up vertically, this corresponds to a region of impact at the upper phase boundary, and therefore enhanced melting. The correlation of the phase boundary evolution and the large-scale convective circulation suggests that future studies of pattern formation by convection and phase change at high *Ra* should consider 3-D domains of very large aspect ratio.

6. Effect of Stefan number *St*

The Stefan number measures the ratio between latent heat and sensible heat. The higher *St* is, the more heat is needed to melt the solid and thus the lower the melt rate. In their previous study, Favier *et al.* (2019) explored the melting in RB convection at $Pr = 1$, $Ra \leq 10^8$ and $0.02 \leq St \leq 50$, and found that *St* plays an insignificant role in the interface roughness amplitude. In our study at $Pr = 10$, with $10^8 \leq Ra \leq 10^{11}$ and $0.1 \leq St \leq 4$, we also find that *St* still has insignificant effects on the roughness amplitude.

In figure 8, we present the roughness amplitude $\tilde{\xi}_{rms}$ as a function of Ra_{eff} as in figure 4(*a*) but now at different *Ra* and *St*. Here, we find that $\tilde{\xi}_{rms}$ shows strong dependence on Ra_{eff} and little dependence on *St* at all of the different *Ra* values; the same observation as in the previous study of Favier *et al.* (2019). Although there are fluctuations of the

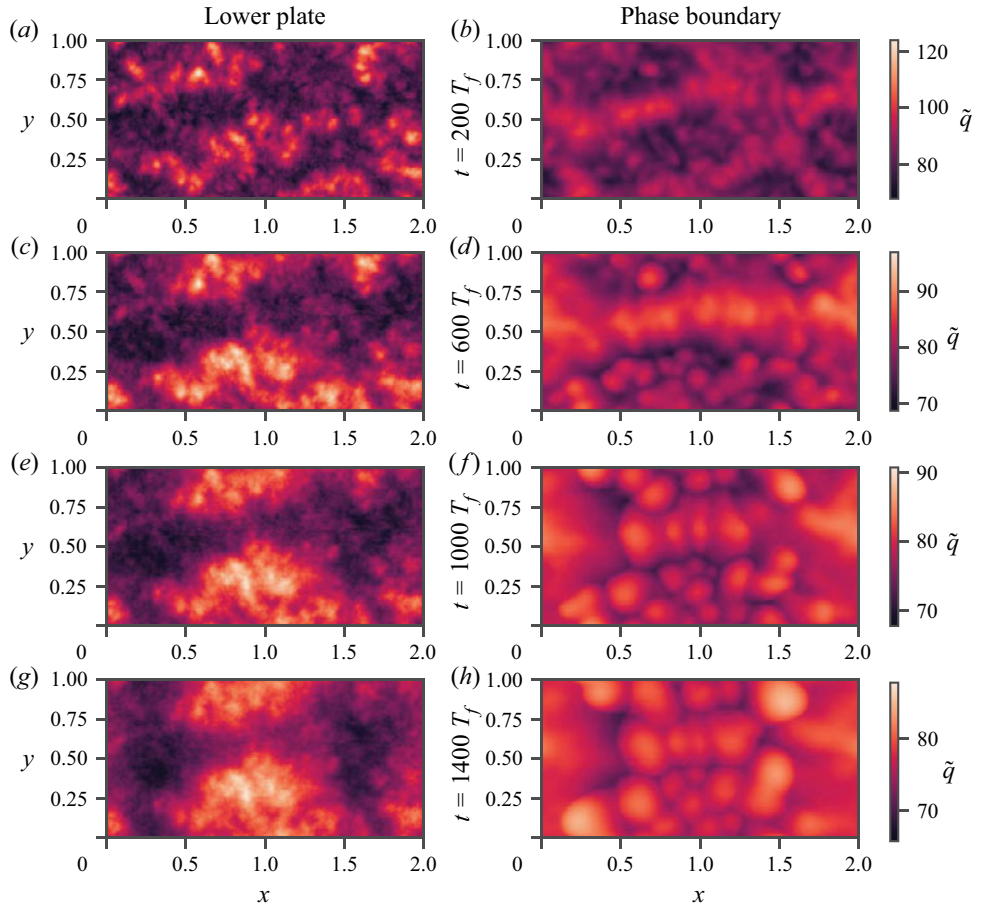

Figure 7. Short-time-integrated heat flux $\tilde{q}(x, y)$ (cf. (5.5)) for the 3-D simulation at $Ra = 10^9$, for the bottom plate $z = 0$ (*a*,*c*,*e*,*g*) and the phase boundary $z = h$ (*b*,*d*,*f*,*h*). Note the similarity of (*d*,*f*,*h*) with those of the topography in figure 1(*e*,*f*,*g*), although times here are slightly different.

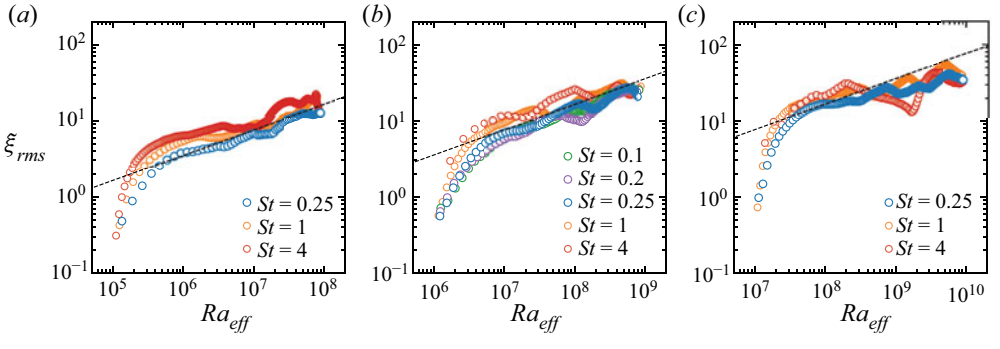

Figure 8. Effect of St on the roughness amplitude $\tilde{\xi}_{rms}$ vs Ra_{eff} for (*a*) $Ra = 10^8$, (*b*) $Ra = 10^9$, (*c*) $Ra = 10^{10}$. The dashed lines represent $\tilde{\xi}_{rms} \sim Ra_{eff}^{1/3}$.

results due to the merging process discussed above, the relation of $\tilde{\xi}_{rms} \sim Ra_{eff}^{1/3}$ can still be clearly seen at different St, similarly to figure 4(a).

7. Conclusions and outlook

We have simulated the melting of a solid above a liquid melt driven by turbulent convection, using direct numerical simulations coupled with the phase-field method in both two and three dimensions. We have shown that the topography becomes rougher as Ra_{eff} increases, and we also explained the mechanism of roughness, which is because of the non-uniform heat flux at the ejecting plume region and impacting plume region. Further, we find the surface roughness amplitude scales with $Ra_{eff}^{1/3}$, and quantitatively derive this scaling relation from the Stefan boundary condition, given measurements obtained for the heat flux distribution at the interface. It also means that the roughness amplitude $h_{rms} \sim \bar{h}$. We quantify the typical horizontal length scale of the convection rolls and the emerging morphology and compare with the theoretical results for the bounds for the width of the convection rolls in Wang *et al.* (2020) for smooth walls, finding good agreement, in spite of the slightly different geometries (smooth plates vs rough upper evolving 'plate'). In three dimensions such bounds are not appropriate, and we find the need for very large aspect ratio domains to capture the full range of scales of the evolving phase boundary. These results highlight the intrinsic coupling between the morphology of the solid and the convective flow structures. Finally, we show that the interface roughness hardly depends on St.

Based on our results, we now have a clearer picture of the topography evolution above turbulent thermal convection. We answer how the topography of a melting solid evolves over turbulent convective flow at higher Rayleigh numbers (up to $Ra = 10^{11}$) than the previous studies at lower Rayleigh numbers (Esfahani *et al.* 2018; Favier *et al.* 2019). Similar cellular structures as in Favier *et al.* (2019) are found in the regions of hot plumes, while rough cellular structures in the regions of cold descending plumes are different from the cusp structures found in Favier *et al.* (2019). This is because that turbulent plumes are able to effectively mix their surroundings, thus inducing an increase of horizontal heat transport and rougher topography.

The main ideas of our results can also be generalized to many natural and industrial applications, such as subglacial lakes (Couston & Siegert 2021), magma oceans (Ulvrová *et al.* 2012) and phase-change materials (Dhaidan & Khodadadi 2015; Noel *et al.* 2022).

Many aspects of this apparently simple system remain to be explored. In many industrial and environmental applications, 3-D simulations at higher Ra and larger aspect ratio are needed, which, however, remain numerically expensive. Also, Pr should also play an important role, which affects the boundary layer thickness (increasing velocity boundary layer width compared with thermal boundary layer for higher Pr) and plume structures. We expect the ice morphology will include more small-scale structures at high Pr. Due to the computational limit, we cannot fully explore the effect of Pr. We also note that for cold water Pr only varies in a small range around 10 according to its only weak temperature dependence. Future research might also compare both melting and freezing processes (through different initial conditions) and address the issue of possible hysteresis and whether multiple states exist. Moreover, the density maximum close to 4 °C in freshwater also plays an important role (Wang *et al.* 2021*e*), which can significantly affect the flow and solid–liquid interface structures (Weady *et al.* 2022). For simplicity, here we assumed a liquid with a linear temperature dependence of the density.

Beyond these studies, future studies should be extended to multi-component liquids such as seawater. For glacial melting in seawater, the density depends on both the temperature and on the salt concentration, which in turn influences the flow structure. And those studies with melting into salty water should also be extended to further canonical geometries, such as vertical convection.

Supplementary movies. Supplementary movies are available at https://doi.org/10.1017/jfm.2023.15.

Acknowledgements. We acknowledge PRACE for awarding us access to MareNostrum in Spain at the Barcelona Computing Center (BSC) under the project 2020235589 and project 2021250115 and the Netherlands Center for Multiscale Catalytic Energy Conversion (MCEC). This work was also carried out on the Dutch national e-infrastructure with the support of SURF Cooperative.

Funding. We acknowledge the support of the Priority Programme SPP 1881 Turbulent Superstructures of the Deutsche Forschungsgemeinschaf.

Declaration of interests. The authors report no conflict of interest.

Author ORCIDs.
Rui Yang https://orcid.org/0000-0002-9870-6743;
Christopher J. Howland https://orcid.org/0000-0003-3686-9253;
Hao-Ran Liu https://orcid.org/0000-0001-7754-9454;
Roberto Verzicco https://orcid.org/0000-0002-2690-9998;
Detlef Lohse https://orcid.org/0000-0003-4138-2255.

References

Ahlers, G., Grossmann, S. & Lohse, D. 2009 Heat transfer and large scale dynamics in turbulent Rayleigh–Bénard convection. *Rev. Mod. Phys.* **81** (2), 503.

Blass, A., Verzicco, R., Lohse, D., Stevens, R.J.A.M. & Krug, D. 2021 Flow organisation in laterally unconfined Rayleigh–Bénard turbulence. *J. Fluid Mech.* **906**, A22.

Cao, Y., Tan, W. & Wu, Z. 2018 Aircraft icing: an ongoing threat to aviation safety. *Aerosp. Sci. Technol.* **75**, 353–385.

Cenedese, C. & Straneo, F. 2023 Icebergs melting. *Annu. Rev. Fluid Mech.* **55**, 377–402.

Chillà, F. & Schumacher, J. 2012 New perspectives in turbulent Rayleigh-Bénard convection. *Eur. Phys. J.* E **35** (7), 58.

Couston, L.-A., Hester, E., Favier, B., Taylor, J.R., Holland, P.R. & Jenkins, A. 2021 Topography generation by melting and freezing in a turbulent shear flow. *J. Fluid Mech.* **911**, A44.

Couston, L.-A. & Siegert, M. 2021 Dynamic flows create potentially habitable conditions in antarctic subglacial lakes. *Sci. Adv.* **7** (8), eabc3972.

Davis, S.H., Müller, U. & Dietsche, C. 1984 Pattern selection in single-component systems coupling Bénard convection and solidification. *J. Fluid Mech.* **144**, 133–151.

Dhaidan, N.S. & Khodadadi, J. 2015 Melting and convection of phase change materials in different shape containers: a review. *Renew. Sustain. Energy Rev.* **43**, 449–477.

Ding, H., Spelt, P.D. & Shu, C. 2007 Diffuse interface model for incompressible two-phase flows with large density ratios. *J. Comput. Phys.* **226** (2), 2078–2095.

Esfahani, B.R., Hirata, S.C., Berti, S. & Calzavarini, E. 2018 Basal melting driven by turbulent thermal convection. *Phys. Rev. Fluids* **3** (5), 053501.

Favier, B., Purseed, J. & Duchemin, L. 2019 Rayleigh–Bénard convection with a melting boundary. *J. Fluid Mech.* **858**, 437–473.

Hester, E.W., Couston, L.-A., Favier, B., Burns, K.J. & Vasil, G.M. 2020 Improved phase-field models of melting and dissolution in multi-component flows. *Proc. R. Soc.* A **476** (2242), 20200508.

Hester, E.W., McConnochie, C.D., Cenedese, C., Couston, L.-A. & Vasil, G. 2021 Aspect ratio affects iceberg melting. *Phys. Rev. Fluids* **6** (2), 023802.

Hewitt, I.J. 2020 Subglacial plumes. *Annu. Rev. Fluid Mech.* **52**, 145–169.

Hohenberg, P.C. & Halperin, B.I. 1977 Theory of dynamic critical phenomena. *Rev. Mod. Phys.* **49** (3), 435.

HOWLAND, C.J. 2022 AFiD-MuRPhFi documentation. Available at: https://chowland.github.io/AFiD-MuRPhFi/.

JENKINS, A., SHOOSMITH, D., DUTRIEUX, P., JACOBS, S., KIM, T.W., LEE, S.H., HA, H.K. & STAMMERJOHN, S. 2018 West antarctic ice sheet retreat in the amundsen sea driven by decadal oceanic variability. *Nat. Geosci.* **11** (10), 733–738.

KAMKARI, B. & AMLASHI, H.J. 2017 Numerical simulation and experimental verification of constrained melting of phase change material in inclined rectangular enclosures. *Intl Commun. Heat Mass Transfer* **88**, 211–219.

KIM, J.-T., NAM, J., SHEN, S., LEE, C. & CHAMORRO, L.P. 2020 On the dynamics of air bubbles in Rayleigh–Bénard convection. *J. Fluid Mech.* **891**, A7.

KOOIJ, G.L., BOTCHEV, M.A., FREDERIX, E.M., GEURTS, B.J., HORN, S., LOHSE, D., VAN DER POEL, E.P., SHISHKINA, O., STEVENS, R.J.A.M. & VERZICCO, R. 2018 Comparison of computational codes for direct numerical simulations of turbulent Rayleigh–Bénard convection. *Comput. Fluids* **166**, 1–8.

KRUG, D., LOHSE, D. & STEVENS, R.J.A.M. 2020 Coherence of temperature and velocity superstructures in turbulent Rayleigh–Bénard flow. *J. Fluid Mech.* **887**, A2.

LABROSSE, S., HERNLUND, J. & COLTICE, N. 2007 A crystallizing dense magma ocean at the base of the Earth's mantle. *Nature* **450** (7171), 866–869.

LAKKARAJU, R., STEVENS, R.J.A.M., ORESTA, P., VERZICCO, R., LOHSE, D. & PROSPERETTI, A. 2013 Heat transport in bubbling turbulent convection. *Proc. Natl Acad. Sci.* **110** (23), 9237–9242.

LIU, H.-R., CHONG, K.L., NG, C.S., VERZICCO, R. & LOHSE, D. 2022*a* Enhancing heat transport in multiphase Rayleigh–Bénard turbulence by changing the plate–liquid contact angles. *J. Fluid Mech.* **933**, R1.

LIU, H.-R., CHONG, K.L., YANG, R., VERZICCO, R. & LOHSE, D. 2022*b* Heat transfer in turbulent Rayleigh–Bénard convection through two immiscible fluid layers. *J. Fluid Mech.* **938**, A31.

LIU, H.-R., NG, C.S., CHONG, K.L., LOHSE, D. & VERZICCO, R. 2021 An efficient phase-field method for turbulent multiphase flows. *J. Comput. Phys.* **446**, 110659.

LOHSE, D. & XIA, K. 2010 Small-scale properties of turbulent Rayleigh-Bénard convection. *Annu. Rev. Fluid Mech.* **42** (1), 335–364.

NOEL, J., METIVIER, C., BECKER, S. & LECLERC, S. 2022 Natural convection in phase change material: experimental study. *Intl J. Heat Mass Transfer* **183**, 122047.

ORESTA, P., VERZICCO, R., LOHSE, D. & PROSPERETTI, A. 2009 Heat transfer mechanisms in bubbly Rayleigh–Bénard convection. *Phys. Rev.* E **80** (2), 026304.

PANDEY, A., SCHEEL, J.D. & SCHUMACHER, J. 2018 Turbulent superstructures in Rayleigh–Bénard convection. *Nat. Commun.* **9** (1), 2118.

VAN DER POEL, E.P., OSTILLA-MÓNICO, R., DONNERS, J. & VERZICCO, R. 2015*a* A pencil distributed finite difference code for strongly turbulent wall-bounded flows. *Comput. Fluids* **116**, 10–16.

VAN DER POEL, E.P., OSTILLA-MÓNICO, R., VERZICCO, R., GROSSMANN, S. & LOHSE, D. 2015*b* Logarithmic mean temperature profiles and their connection to plume emissions in turbulent Rayleigh–Bénard convection. *Phys. Rev. Lett.* **115** (15), 154501.

PURSEED, J., FAVIER, B., DUCHEMIN, L. & HESTER, E.W. 2020 Bistability in Rayleigh–Bénard convection with a melting boundary. *Phys. Rev. Fluids* **5** (2), 023501.

RAVICHANDRAN, S. & WETTLAUFER, J.S. 2021 Melting driven by rotating Rayleigh–Bénard convection. *J. Fluid Mech.* **916**, A28.

REITER, P., SHISHKINA, O., LOHSE, D. & KRUG, D. 2021 Crossover of the relative heat transport contributions of plume ejecting and impacting zones in turbulent Rayleigh–Bénard convection (a). *Europhys. Lett.* **134** (3), 34002.

RISTROPH, L. 2018 Sculpting with flow. *J. Fluid Mech.* **838**, 1–4.

RUBINSTEIN, L. 1971 *The Stefan Problem*. American Mathematical Society.

SHISHKINA, O. 2021 Rayleigh–Bénard convection: the container shape matters. *Phys. Rev. Fluids* **6** (9), 090502.

SIVASAMY, P., DEVARAJU, A. & HARIKRISHNAN, S. 2018 Review on heat transfer enhancement of phase change materials (PCMs). *Mater. Today: Proc.* **5** (6), 14423–14431.

SPENCER, J., PEARL, J., SEGURA, M., FLASAR, F., MAMOUTKINE, A., ROMANI, P., BURATTI, B., HENDRIX, A., SPILKER, L. & LOPES, R. 2006 Cassini encounters enceladus: background and the discovery of a south polar hot spot. *Science* **311** (5766), 1401–1405.

STANTON, T.P., SHAW, W., TRUFFER, M., CORR, H., PETERS, L., RIVERMAN, K., BINDSCHADLER, R., HOLLAND, D. & ANANDAKRISHNAN, S. 2013 Channelized ice melting in the ocean boundary layer beneath Pine Island Glacier, Antarctica. *Science* **341** (6151), 1236–1239.

ULVROVÁ, M., LABROSSE, S., COLTICE, N., RABACK, P. & TACKLEY, P. 2012 Numerical modelling of convection interacting with a melting and solidification front: application to the thermal evolution of the basal magma ocean. *Phys. Earth Planet. Inter.* **206**, 51–66.

VERZICCO, R. & ORLANDI, P. 1996 A finite-difference scheme for three-dimensional incompressible flows in cylindrical coordinates. *J. Comput. Phys.* **123** (2), 402–414.

WANG, Z., CALZAVARINI, E. & SUN, C. 2021*a* Equilibrium states of the ice-water front in a differentially heated rectangular cell (a). *Europhys. Lett.* **135** (5), 54001.

WANG, Z., CALZAVARINI, E., SUN, C. & TOSCHI, F. 2021*b* How the growth of ice depends on the fluid dynamics underneath. *Proc. Natl Acad. Sci.* **118**, 10.

WANG, Z., JIANG, L., DU, Y., SUN, C. & CALZAVARINI, E. 2021*c* Ice front shaping by upward convective current. *Phys. Rev. Fluids* **6** (9), L091501.

WANG, Q., LOHSE, D. & SHISHKINA, O. 2021*d* Scaling in internally heated convection: a unifying theory. *Geophys. Res. Lett.* **48** (4), e2020GL091198.

WANG, Z., MATHAI, V. & SUN, C. 2019 Self-sustained biphasic catalytic particle turbulence. *Nat. Commun.* **10** (1), 1–7.

WANG, Q., REITER, P., LOHSE, D. & SHISHKINA, O. 2021*e* Universal properties of penetrative turbulent Rayleigh–Bénard convection. *Phys. Rev. Fluids* **6** (6), 063502.

WANG, S.L., SEKERKA, R.F., WHEELER, A.A., MURRAY, B.T., CORIELL, S.R., BRAUN, R.J. & MCFADDEN, G.B. 1993 Thermodynamically-consistent phase-field models for solidification. *Phys.* D **69** (1-2), 189–200.

WANG, Q., VERZICCO, R., LOHSE, D. & SHISHKINA, O. 2020 Multiple states in turbulent large-aspect-ratio thermal convection: what determines the number of convection rolls? *Phys. Rev. Lett.* **125** (7), 074501.

WEADY, S., TONG, J., ZIDOVSKA, A. & RISTROPH, L. 2022 Anomalous convective flows carve pinnacles and scallops in melting ice. *Phys. Rev. Lett.* **128** (4), 044502.

WOODS, A.W. 1992 Melting and dissolving. *J. Fluid Mech.* **239**, 429–448.

WORSTER, M.G., BATCHELOR, G. & MOFFATT, H. 2000 Solidification of fluids. *Perspectives Fluid Dyn.* **742**, 393–446.

XIE, Y.-C. & XIA, K.-Q. 2013 Dynamics and flow coupling in two-layer turbulent thermal convection. *J. Fluid Mech.* **728**, R1.

YANG, R., CHONG, K.L., WANG, Q., VERZICCO, R., SHISHKINA, O. & LOHSE, D. 2020 Periodically modulated thermal convection. *Phys. Rev. Lett.* **125** (15), 154502.

YANG, Y., VERZICCO, R. & LOHSE, D. 2016 From convection rolls to finger convection in double-diffusive turbulence. *Proc. Natl Acad. Sci.* **113**, 69–73.

YUE, P., ZHOU, C. & FENG, J.J. 2010 Sharp-interface limit of the Cahn–Hilliard model for moving contact lines. *J. Fluid Mech.* **645**, 279–294.

ZHONG, J.-Q., FUNFSCHILLING, D. & AHLERS, G. 2009 Enhanced heat transport by turbulent two-phase Rayleigh–Bénard convection. *Phys. Rev. Lett.* **102** (12), 124501.

ZHU, X., MATHAI, V., STEVENS, R.J.A.M., VERZICCO, R. & LOHSE, D. 2018 Transition to the ultimate regime in two-dimensional Rayleigh–Bénard convection. *Phys. Rev. Lett.* **120** (14), 144502.